

A Comparative Study of 2D Numerical Methods with GPU Computing

Ben J. Zimmerman, Jonathan D. Regele*, & Bong Wie

Department of Aerospace Engineering, Iowa State University, Ames, IA 50011, USA

* Corresponding author: jregele@lanl.gov

September 3, 2018

Abstract

Graphics Processing Unit (GPU) computing is becoming an alternate computing platform for numerical simulations. However, it is not clear which numerical scheme will provide the highest computational efficiency for different types of problems. To this end, numerical accuracies and computational work of several numerical methods are compared using a GPU computing implementation. The Correction Procedure via Reconstruction (CPR), Discontinuous Galerkin (DG), Nodal Discontinuous Galerkin (NDG), Spectral Difference (SD), and Finite Volume (FV) methods are investigated using various reconstruction orders. Both smooth and discontinuous cases are considered for two-dimensional simulations. For discontinuous problems, MUSCL schemes are employed with FV, while CPR, DG, NDG, and SD use slope limiting. The computation time to reach a set error criteria and total time to complete solutions are compared across the methods. It is shown that while FV methods can produce solutions with low computational times, they produce larger errors than high-order methods for smooth problems at the same order of accuracy. For discontinuous problems, the methods show good agreement with one another in terms of solution profiles, and the total computational times between FV, CPR, and SD are comparable.

Keywords: High-order methods; Finite Volume; GPU computing; CUDA

1 Introduction

Numerical simulation of fluids typically requires high resolution and large computational power. In industrial settings, high resolution is usually obtained through the computational domain, and not the computational method itself. This is because low-order methods such as finite volume (FV) are employed in simulations. In this paper, a low-order method implies either 1^{st} or 2^{nd} order spatial reconstruction, while a high-order method indicates a solution reconstruction of 3^{rd} order and higher [1]. This differs from compressible methods, where a low-order method is 1^{st} order accurate, and high-order is 2^{nd} or 3^{rd} order accurate. While it is possible for FV methods to achieve higher-order spatial reconstruction, the computational cost becomes high in terms of memory access, especially for unstructured grids [2]. The solution reconstruction requires information from neighboring elements, and as the order of accuracy is increased, the number of elements required for communication also increases. In contrast, high-order methods only require information at element neighbors, regardless of the order of accuracy. This compact nature is appealing to parallel processing, especially Graphics Processing Unit (GPU) computing.

While most practical computations are completed in three-dimensions, two-dimensional problems are still of interest. They are even more appealing towards GPUs, whose low memory storage makes computing on high-resolution three-dimensional problems a issue. In addition, it is not clear how different numerical methods compare with one-another under GPU implementation, even for

two-dimensional problems. Various researchers have explored GPU Compute Unified Device Architecture (CUDA) with different numerical methods. Implementation of the FV method for GPUs has been investigated by Castro *et al.* [3], where the governing equations were the shallow water equations, and Obenschain [4] for unstructured meshes. The parallelism of FV per element is limited, as solutions are reconstructed along element edges before the volume integration step. In contrast, high-order methods have multiple solution states within each element, stored at solution points, which increases parallelism per element. The most developed high-order methods to date include Discontinuous Galerkin (DG), Nodal Discontinuous Galerkin (NDG), Correction Procedure via Reconstruction (CPR), and Spectral Difference (SD).

Discontinuous Galerkin (DG) [5, 6, 7, 8, 9, 10] was the first high-order method introduced to hyperbolic equations. There are multiple approaches to the DG method, depending on how the integration points are chosen. Using Gauss-Legendre points for DG implementation demands computations of surface and volume integrals at each step. This allows for improved accuracy at a cost of increased computational work per step. A more efficient implementation of DG was completed by Hesthaven and Warburton [11], which moved the integration points to element edges (NDG). For an in depth discussion of the implementation of NDG to GPUs, the reader is directed to the paper by Klöckner *et al.* [12]. The CPR method was developed to improve efficiency of other high-order methods [13, 14, 15, 16], which includes the DG method. The CPR approach allows the equations to be solved in differential form, removing the added surface and volume integration computations present in DG. While this increases the computing speed, the method is not as accurate as the DG approach [1]. CPRs application to GPUs was completed by Hoffmann and Zimmerman [17, 18], where significant speed-ups are observed. The SD method is a finite difference-like formulation [19, 20, 21], which uses two sets of points, solution and flux points, where the flux derivative is computed across the flux points to update the solution states. The SD methods application to GPUs was completed by Zimmerman [22] for a three-dimensional system.

The aforementioned references layout efficient algorithms and implementation techniques for the numerical methods discussed, and compare the speeds from GPU to Central Processing Unit (CPU) implementations, where significant speed-up results are shown. There has been a comparative study done by Yu *et al.* [23] on high-order methods using a CPU platform. However, there has been no performance assessment of different methods using a GPU platform. Furthermore, there has been no performance comparison between high-order methods to FV methods on GPUs. Thus, the intent of this paper is to perform a fair comparison in two-dimensions of numerical methods and determine the relative performance between them in terms of total computing speed and accuracy with GPUs. The developed approach for two-dimensions should be extended to three-dimensions in subsequent work in order to account for the known shift in computational cost from two to three-dimensions. To this end, the FV, CPR, DG, NDG, and SD methods are all implemented using GPU CUDA, in similar manners from the references discussed above. Each method is compared at the same order of accuracy and same number of degrees of freedom, with the maximum allowable time-step for a given mesh. The comparison is for the two-dimensional Euler system, for both smooth and discontinuous problems. For discontinuous problems, a shock capturing approach is required. For the FV method, the MUSCL scheme [24, 25, 26] is implemented, while the high-order methods use a slope limiter [7] to limit the order of the solution only at discontinuities. The present study investigates only quadrilateral elements, where the total number of degrees of freedom are held constant between the methods. In addition, each method takes a maximum allowable time-step for stability. This plays an important factor when considering the work to reach a specified final time, since high-order methods are time-step restricted, and this restriction increases with the order of accuracy of the scheme [27, 28].

The paper is organized in the following manner. In section 2, each numerical method implemented is discussed briefly. Section 3 outlines the implementation with GPU programming. The results are discussed in section 4, where error analysis and computational time information are discussed in detail. Finally, section 5 draws conclusions from the study.

2 Numerical Methods

The hyperbolic conservation law is given by,

$$\frac{\partial \mathbf{q}}{\partial t} + \vec{\nabla} \cdot \vec{\mathbf{F}}(\mathbf{q}) = 0, \quad (1)$$

where \mathbf{q} is the state vector and $\vec{\nabla} \cdot \vec{\mathbf{F}}(\mathbf{q})$ is the divergence of the inviscid flux vector, which takes the following form,

$$\vec{\nabla} \cdot \vec{\mathbf{F}}(\mathbf{q}) = \frac{\partial \mathbf{f}(\mathbf{q})}{\partial x} + \frac{\partial \mathbf{g}(\mathbf{q})}{\partial y}. \quad (2)$$

For the two-dimensional Euler equations, \mathbf{q} is a vector of the conserved variables,

$$\mathbf{q} = \begin{bmatrix} \rho \\ \rho u \\ \rho v \\ e \end{bmatrix}, \quad (3)$$

and $\mathbf{f}(\mathbf{q})$ and $\mathbf{g}(\mathbf{q})$ are flux vectors,

$$\mathbf{f}(\mathbf{q}) = \begin{bmatrix} \rho u \\ p + \rho u^2 \\ \rho uv \\ u(e + p) \end{bmatrix}, \quad \mathbf{g}(\mathbf{q}) = \begin{bmatrix} \rho v \\ \rho uv \\ p + \rho v^2 \\ v(e + p) \end{bmatrix}. \quad (4)$$

In Eqns. (3) and (4), ρ is the density, u is the x-direction velocity, v is the y-direction velocity, e is the total energy per unit volume, and p is the pressure. To close the system, the ideal gas equation of state is used,

$$p = (\gamma - 1)(e - \frac{1}{2}\rho(u^2 + v^2)). \quad (5)$$

The computational domain is discretized with non-overlapping elements, each with volume V_m . Additionally, each element must be transformed into a standard element [29]. Within each element, a set of solution points are defined, which stores the solution states.

2.1 FV Formulation

In the FV approach, the solution per element takes on an averaged value. The governing equations are integrated over the elements volume, V_m ,

$$\int_{V_m} \left[\frac{\partial \mathbf{q}}{\partial t} + \vec{\nabla} \cdot \vec{\mathbf{F}}(\mathbf{q}) \right] dV = 0. \quad (6)$$

The solution average, denoted by $\bar{\mathbf{q}}_m$ is then defined as

$$\bar{\mathbf{q}}_m = \frac{1}{V_m} \int_{V_m} \bar{\mathbf{q}} dV. \quad (7)$$

The semi-discretization can then be written in the following well known form for two-dimensional quadrilateral elements,

$$\frac{\partial \bar{\mathbf{q}}_{i,j}}{\partial t} + \frac{1}{\Delta x} [\mathbf{f}_{i+1/2,j} - \mathbf{f}_{i-1/2,j}] + \frac{1}{\Delta y} [\mathbf{g}_{i,j+1/2} - \mathbf{g}_{i,j-1/2}] = 0. \quad (8)$$

In the above formulation, i is the index in the x-direction, while j is the index in the y-direction. To obtain the flux at an interface (say $\mathbf{f}_{i-1/2,j}$, which is the left interface of the element) left and right solutions need to be reconstructed at the elements edge first. Once left and right solutions are found at each interface, a Riemann problem is solved to determine the flux value at the interface. The averaged solution is then updated via a time-marching scheme.

2.2 CPR Formulation

Here, the CPR method is described. For a full derivation, see [14]. The formulation of the CPR method requires the definition of an arbitrary weighting function w . By multiplying the weighting function to Eqn. (1) and integrating over the domain, Eqn. (1) becomes

$$\int_{V_m} \left[\frac{\partial \mathbf{q}}{\partial t} + \vec{\nabla} \cdot \vec{\mathbf{F}}(\mathbf{q}) \right] w dV = 0. \quad (9)$$

By applying the Gauss divergence theorem, Eqn. (9) is expanded to be

$$\int_{V_m} \frac{\partial \mathbf{q}}{\partial t} w dV + \int_{\partial V_m} w \vec{\mathbf{F}}(\mathbf{q}) \cdot \mathbf{n} dS - \int_{V_m} \vec{\nabla} w \cdot \vec{\mathbf{F}}(\mathbf{q}) dV = 0. \quad (10)$$

Let \mathbf{q}_m approximate the solution \mathbf{q} within the element V_m . Furthermore, the solution is assumed to belong to the space of polynomials of degree k or less ($\mathbf{q}_m \in P^k$). Thus, Eqn. (10) must satisfy the following,

$$\int_{V_m} \frac{\partial \mathbf{q}_m}{\partial t} w dV + \int_{\partial V_m} w \vec{\mathbf{F}}(\mathbf{q}_m) \cdot \mathbf{n} dS - \int_{V_m} \vec{\nabla} w \cdot \vec{\mathbf{F}}(\mathbf{q}_m) dV = 0. \quad (11)$$

There is no requirement enforced on element edges at this point. The normal flux is replaced with a common Riemann flux to enforce element coupling,

$$\int_{V_m} \frac{\partial \mathbf{q}_m}{\partial t} w dV + \int_{\partial V_m} w \vec{\mathbf{F}}_{com}^n(\mathbf{q}_m, \mathbf{q}_{m+}) dS - \int_{V_m} \vec{\nabla} w \cdot \vec{\mathbf{F}}(\mathbf{q}_m) dV = 0. \quad (12)$$

In Eqn. (12), \mathbf{q}_{m+} is the solution outside of element m . Next, integration by parts is applied again to the last term in Eqn. (12) to yield

$$\int_{V_m} \frac{\partial \mathbf{q}_m}{\partial t} w dV + \int_{V_m} w \vec{\nabla} \cdot \vec{\mathbf{F}}(\mathbf{q}_m) dV + \int_{\partial V_m} w [\mathbf{F}_{com}^n - \mathbf{F}^n(\mathbf{q}_m)] dS = 0. \quad (13)$$

In the CPR formulation, the last term in Eqn. (13) is viewed as a penalty term, which can be lifted to a volume integral by introducing a correction polynomial $\delta_m \in P^k$,

$$\int_{V_m} w \delta_m dV = \int_{\partial V_m} w [\mathbf{F}_{com}^n - \mathbf{F}^n(\mathbf{q}_m)] dS. \quad (14)$$

The volume integral formulation of Eqn. (13) is obtained,

$$\int_{V_m} \left[\frac{\partial \mathbf{q}_m}{\partial t} + \vec{\nabla} \cdot \vec{\mathbf{F}}(\mathbf{q}_m) + \delta_m \right] w dV = 0. \quad (15)$$

If the conservation law is non-linear, then $\vec{\nabla} \cdot \vec{\mathbf{F}}(\mathbf{q}_m)$ does not generally fall into P^k . To resolve the non-linear situation, the term $\vec{\nabla} \cdot \vec{\mathbf{F}}(\mathbf{q}_m)$ is projected into P^k . Then, eliminating the weight and volume integral gives the differential formulation,

$$\frac{\partial \mathbf{q}_m}{\partial t} + \Pi \left[\vec{\nabla} \cdot \vec{\mathbf{F}}(\mathbf{q}_m) \right] + \delta_m = 0. \quad (16)$$

The weighted residual formulation is reduced to a differential one. Each element must store the solution states at a set of points, called solution points. For the CPR method, within an element V_m , a set of Legendre-Lobatto solution points are defined, as shown in Fig. 1 (b). At each solution point j , Eqn. (16) must be true,

$$\frac{\partial \mathbf{q}_{m,j}}{\partial t} + \Pi_j \left[\vec{\nabla} \cdot \vec{\mathbf{F}}(\mathbf{q}_m) \right] + \delta_{m,j} = 0. \quad (17)$$

Now the calculation of both $\Pi_j \left[\vec{\nabla} \cdot \vec{\mathbf{F}}(\mathbf{q}_m) \right]$ and the correction polynomial, $\delta_{m,j}$, must be completed. The inviscid flux divergence follows a chain rule approach (see [30] for analytical flux derivative). For δ_m formulations, see [15]. In this work, the correction polynomial is computed using Radau polynomials, which casts δ into the DG framework [13], improving accuracy. The definition of Legendre-Lobatto solution points brings a sense of efficiency into the method. The solution points occupy edges of elements, thus no interpolation of information to element edges is required, and element coupling becomes straightforward.

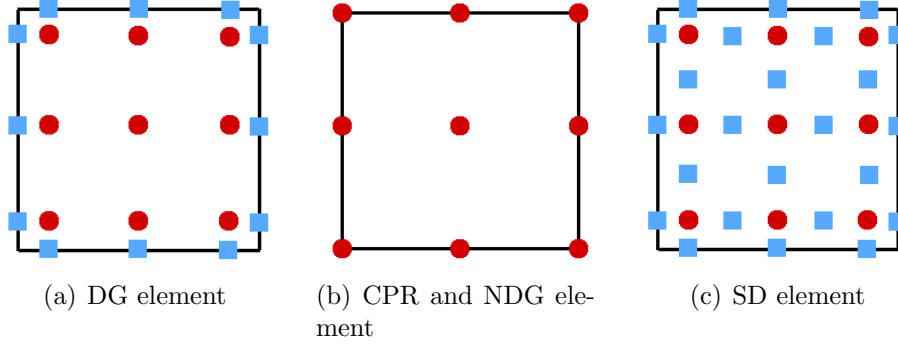


Figure 1: Solution points (red circles) and flux points (blue squares) locations for P^2 solution reconstruction. (a) Gauss-Legendre solution points with Gauss-Lobatto interface points. Associated with the DG method. (b) Gauss-Lobatto solution points with coinciding flux points. Associated with CPR and NDG methods. (c) Gauss-Legendre solution points with Gauss-Lobatto flux points. Associated with SD method.

2.3 DG Formulation

The DG methods formulation is more straightforward than the CPR method, and more information can be found in Ref. [7]. Again, a weighting function w multiplies the conservation law, Eqn. (1), and is integrated over the domain,

$$\int_{V_m} \left[\frac{\partial \mathbf{q}}{\partial t} + \vec{\nabla} \cdot \vec{\mathbf{F}}(\mathbf{q}) \right] w dV = 0. \quad (18)$$

Like the CPR method, integration by parts is performed, and \mathbf{q}_m , which belongs to the space P^k , is allowed to approximate the solution on element V_m ,

$$\int_{V_m} \frac{\partial \mathbf{q}_m}{\partial t} w dV + \int_{\partial V_m} w \vec{\mathbf{F}}(\mathbf{q}_m) \cdot \mathbf{n} dS - \int_{V_m} \vec{\nabla} w \cdot \vec{\mathbf{F}}(\mathbf{q}_m) dV = 0. \quad (19)$$

The solution and flux polynomials are approximated within each element i over n Gauss-Legendre points as,

$$\mathbf{q}_m = \sum_{j=1}^n \mathbf{q}_{m,j} \phi_j, \quad (20)$$

$$\vec{\mathbf{F}}(\mathbf{q}_{m,j}) = \sum_{j=1}^n \vec{\mathbf{F}}_{m,j} \phi_j, \quad (21)$$

where ϕ_j are the basis functions. If the basis and weighting functions are equal, then the procedure is Galerkin. The surface integral term in Eqn. (19) couples elements together and the common flux is again calculated via a Riemann solver. Since the solution points are Gauss-Legendre for the DG method, there is more computational work per time step when compared to the CPR method, since solutions must be interpolated to edges before element coupling. Figure 1 (a) shows a typical P^2 DG element, where sets of flux points are defined along the edges to communicate solutions. In addition to the interpolation step, volume and surface integral calculations further increase the computational cost of the method.

2.4 NDG Formulation

The Nodal DG formulation closely follows the CPR formulation discussed previously. Equation (1) is multiplied by a weighting function and integrated to yield the weak form,

$$\int_{V_m} \frac{\partial \mathbf{q}_m}{\partial t} w dV + \int_{\partial V_m} w \vec{\mathbf{F}}(\mathbf{q}_m) \cdot \mathbf{n} dS - \int_{V_m} \vec{\nabla} w \cdot \vec{\mathbf{F}}(\mathbf{q}_m) dV = 0. \quad (22)$$

A Riemann flux is used to apply element coupling, and replaces $\vec{F}(\mathbf{q}_m) \cdot \mathbf{n}$ with a common Riemann flux \mathbf{F}_{com}^n , which uses the current and neighboring element information,

$$\int_{V_m} \frac{\partial \mathbf{q}_m}{\partial t} w dV + \int_{\partial V_m} w \mathbf{F}_{com}^n dS - \int_{V_m} \vec{\nabla} w \cdot \vec{F}(\mathbf{q}_m) dV = 0. \quad (23)$$

For the DG approach, a basis set w_j is chosen for the solution space, where j is the index of each solution point. Equation (23) is written as the following strong DG form,

$$\frac{\partial}{\partial t} \int_{V_m} w_i \mathbf{q}_{m,j} w_j dV - \int_{\partial V_m} w_i \left[\vec{F} \cdot \mathbf{n} - \mathbf{F}_{com}^n \right] dS + \int_{V_m} w_i \vec{\nabla} \cdot \vec{F}(\mathbf{q}_m) dV = 0. \quad (24)$$

A mass, stiffness, differentiation, and face mass matrices can be formulated, as completed in [12],

$$M_{i,j} = \int_{V_m} w_i w_j dV, \quad (25)$$

$$S_{i,j} = \int_{V_m} w_i \nabla w_j dV, \quad (26)$$

$$D_{i,j} = (M_{i,j})^{-1} S_{i,j}, \quad (27)$$

$$M_{i,j}^A = \int_{\partial V_m} w_i w_j dS. \quad (28)$$

These matrices are used in Eqn. (24) to obtain the following formulation,

$$\frac{\partial \mathbf{q}_{m,j}}{\partial t} + D \left[\vec{F}(\mathbf{q}_m) \right] - L \left[\vec{F} \cdot \mathbf{n} - \mathbf{F}_{com}^n \right]_A = 0. \quad (29)$$

The matrix L , or lifting matrix, acts on the facial degrees of freedom on face A_m . It combines the mathematical aspects of applying the mass matrix on the face, lifting the facial integral to volume integral, and finally applying the inverse mass matrix. Much like CPR, this method also uses Gauss-Lobatto quadrature as the solution points (see Fig. 1 (b)), simplifying the element communication step.

2.5 SD Formulation

The SD scheme employs a finite-difference like approach on the conservation laws. The solution is assumed to be in the space P^k , while the flux is assumed to be in the space P^{k+1} . A set of solution points and flux points are defined within each element. Figure 1 (c) illustrates the point locations in a SD P^2 element. Note how an extra flux point is required per direction for the flux polynomial. The solution states are stored at the solution points while the flux points compute the flux terms. Let $h(\xi)$ define the degree k Lagrange polynomial at the solution points and $l(\xi)$ be the degree $(k+1)$ polynomial at the flux points. The coordinates (x, y) are transformed into standard coordinates (ξ, η) . The solution is reconstructed as tensor products of two one-dimensional polynomials,

$$\mathbf{q} = \sum_{j=1}^{k+1} \sum_{i=1}^{k+1} \mathbf{q}_{i,j} h_i(\xi) h_j(\eta). \quad (30)$$

In a similar manner, the reconstructed flux polynomials are formulated as

$$\mathbf{f} = \sum_{j=1}^{k+1} \sum_{i=0}^{k+1} \mathbf{f}_{i+1/2,j} l_{i+1/2}(\xi) h_j(\eta), \quad (31)$$

$$\mathbf{g} = \sum_{j=0}^{k+1} \sum_{i=1}^{k+1} \mathbf{g}_{i,j+1/2} h_i(\xi) l_{j+1/2}(\eta). \quad (32)$$

In this formulation, i and j indicate the points in x and y directions respectfully. The flux polynomials are only continuous within each element. To resolve the discontinuous interface, a Riemann solver is applied at flux points on the interfaces to provide element coupling. Once the fluxes at the interface are augmented to a common value, the flux derivatives are evaluated as

$$\frac{\partial \mathbf{f}}{\partial \xi} = \sum_{r=0}^{k+1} \mathbf{f}_{r+1/2,j} l'_{r+1/2}(\xi_i), \quad (33)$$

$$\frac{\partial \mathbf{g}}{\partial \eta} = \sum_{r=0}^{k+1} \mathbf{f}_{i,r+1/2} l'_{r+1/2}(\eta_j). \quad (34)$$

The term $l'(\xi_i)$ is the derivative of the flux points lagrange polynomial evaluated at the solution point locations ξ_i .

2.6 Shock Capturing

To resolve solution discontinuities, the low-order and high-order methods follow two approaches. For the FV method, the second and third order MUSCL schemes are implemented, which is applied during the reconstruction of the solution at element interfaces. The slopes of the reconstructed solutions are limited with the *minmod* limiter [31]. For second order reconstruction, the second order MUSCL scheme is applied, while the third order MUSCL scheme is selected for third order reconstruction.

For the high-order methods, the same technique is applied for all schemes, which uses a *minmod* limiter (similar to FV) to find troubled elements and apply slope limiting. The updated solution is interpolated (if need be) to element edges. Once interpolation is completed, the *minmod* limiter is applied to reconstruct a second solution based on cell averaged values to the edge. If the difference in these two values is greater than a certain threshold (numerical experiments indicate $> 1.0 \times 10^{-3}$ gives good solutions) then the cell is marked for limiting, where the new solution is,

$$\mathbf{q}_{m,j} = \bar{\mathbf{q}}_m + (x_{m,j} - x_0) \text{minmod} \left(\frac{\bar{\mathbf{q}}_{m+1} - \bar{\mathbf{q}}_m}{h}, \frac{\bar{\mathbf{q}}_m - \bar{\mathbf{q}}_{m-1}}{h} \right). \quad (35)$$

In Eqn. (35), $\mathbf{q}_{m,j}$ is the solution in element m and solution point j , $x_{m,j}$ is the location of the solution point, x_0 is the element midpoint, h is the element size, and $\bar{\mathbf{q}}_m$ is the averaged solution in an element. This scheme results in a second order reconstruction which can be applied to any of the high-order methods discussed in this paper.

3 GPU CUDA Overview and Implementation

Before discussing the implementation of methods into GPU CUDA, a brief overview of GPU computing is presented, to give the reader a basic understanding of some conventions and algorithms on the GPU. For a more complete discussion, refer to the NVIDIA CUDA programming guide [32].

3.1 CUDA Overview

Graphics computing is aimed toward image rendering, a largely parallel task. GPUs are built around streaming multiprocessors to complete tasks, which execute hundreds of independent threads. The multiprocessors launch blocks, containing threads, running in parallel. Threads within a block are allowed to share information through the GPU's shared memory (each GPU has a limit on the amount of shared memory available). This architecture is coined as single-instruction-multiple-thread (SIMT) architecture. The blocks are executed through a grid, where no communication is allowed between the threads, and there is no guarantee of which block will finish first. Only after every blocks work is completed can the grid be viewed, and data can be analyzed or seen by other threads if the appropriate memory was written into a GPU's global memory. Global memory can be seen by all threads in all blocks on the GPU, and every thread can write to this

memory. However, the cost to write to this memory location can be high (hundreds of clock cycles). So writes into this memory should be completed only when necessary. Global memory can be bound to texture memory to hasten read access. In this implementation, all global memory is also allotted space in the texture memory. Finally, shared memory is used when threads in a block need to communicate information to one another. Typical usage of this occurs during for loops, where one thread needs the information of other threads to perform computations, such as derivatives.

There are a few rules to follow when writing CUDA code to help optimize computing speed.

- The usage of shared memory should be minimized and reused when possible.
- The storage locations of memory should compliment the SIMT architecture.
- Threads should be synchronized rarely and in optimal locations.
- Each thread should write to global memory only once.

Some are quite obvious, such as the recycling of shared memory and location of barriers. For storage order of memory, consider the following case: Let's use the Euler system and assume a memory storage where at a single point, memory position 0 is conservation of mass, memory position 1 and 2 are conservation of momentum in x and y, and memory position 3 is conservation of energy. Now, let thread 0 read memory position 0, thread 1 read memory position 1, and so on. One can observe that evaluating components of the field is completed by evaluating different expressions, which means different code, inefficient for SIMT architecture. A better solution is to let thread 0 access memory position 0 of the point, and thread 1 access the memory position 0 of another point, which allows the same expression to be computed by the threads. The final item, one global write, is also self explanatory, since each access to global memory is expensive. It is noted, however, that in some cases this cannot be followed, and allowing multiple writes to global is cheaper than splitting the algorithm.

Some conventions are now listed to simplify the algorithms presented, and assist the reader. Threads and blocks are allowed to be multi-dimensional, and have the indexes $t_x, t_y, t_z, b_x,$ and b_y (threads can have three indexes while blocks can have up to two). Memory locations are presented in the following manner: Assume some code variable u , which can be in any of the following memory locations based on the superscript. If the variable has no superscript, it resides in the local memory to the thread. The other three locations are denoted by superscripts $g, t,$ and s to represent global, texture, and shared memory space respectfully. In addition, any memory reads or writes with indexes will be denoted in the following manner: If stored memory needs to be read (say c is the pointer or array which holds the information), and the indexes depend on $i, j,$ and k , then let $v = c[(i, j, k)]$. Meaning, v now reads information in c at an index location which depends on $i, j,$ and k (not a three dimensional array or pointer).

3.2 CUDA Implementation

Now that the basic idea is presented, the GPU implementation of each method is presented. Each methods entire implementation will not be discussed, only the residual update and shock capturing algorithm. The remaining functions were implemented according to the algorithms found in Ref. [33]. An overview of each method's steps are outlined in Fig. 2. For each method, the local and non-local operations are shown. A local operation means all information to complete the operation is contained within the element, while non-local means communication must occur between elements. Note that the number of operations listed does nor correlate with the number of functions required. Some operations, local and non-local, can be combined into one function to reduce memory loading and multiple sweeps through the domain.

3.3 FV CUDA

The FV method can be separated into two separate kernels to update the residual. As shown in Fig. 2, one kernel reconstructs the solution and provides element coupling (both non-local operations) whose output feeds into the flux differentiation kernel. The *FV_Reconstruct* algorithm is outlined in Algorithm 1, which reconstructs the left and right solutions at faces and computes the Riemann flux at the face. Our implementation uses strictly texture memory and registers, with one write to global memory to finish the

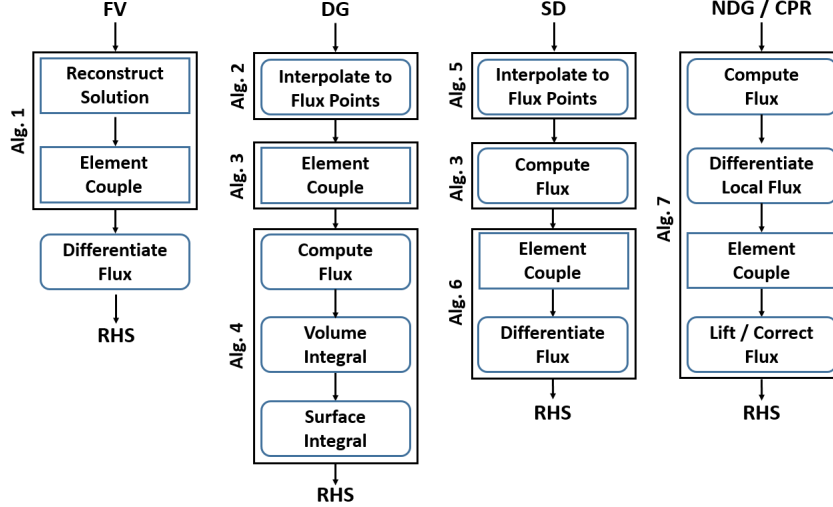


Figure 2: Overview of methods. Rectangles indicate non-local operations, while other shapes indicate local operations.

algorithm. The threads are defined as faces, t_x , in the domain. In all algorithms, multiple elements (or faces) are calculated in one block, increasing the parallelism of the algorithm. The variables n_v and n_e denote the number of state variables and number of elements respectively. Depending on the degree of the reconstruction polynomial, an appropriate amount of information from neighbors is loaded (the index e_1 denotes element 1). Once the data is loaded, the appropriate reconstruction formula is applied and the flux at the interface is computed and stored.

To compute the flux derivative, multiple elements are computed per block, and each thread reads the appropriate flux information from texture memory to compute the flux derivative in the element (computed from *FV_Reconstruct*). The FV method, while simplistic, demands memory transfers from neighboring elements in the domain, which is the major bottleneck in the method.

3.4 High-Order Methods CUDA

For GPU implementation of each high-order method, a general algorithm is presented to compute the flux derivative. The CPR and NDG methods will be lumped together, as implementation of the two is quite similar. The variables n_{sp1d} , n_{fp1d} , n_{sp} , n_{fp} , and n_{ep} denote the number of solution points in one dimension, number of flux points in one dimension, total number of solution points in an element, total number of flux points in an element, and total number of edge points respectively.

3.4.1 DG CUDA

As shown in Fig. 2, the decomposition of the DG residual update requires three kernels. The three algorithms (corresponding to three kernels) interpolate the information from solution points to flux points on element edges, couple the elements via a Riemann flux, and compute the volume and surface integrals using information stored at both solution and flux points.

Algorithm 1 FV_Reconstruct

▷ Faces in element
 $t_x = \text{threadIdx.x}$
▷ Current global face
 $k = \text{blockIdx.x} * \text{blockDim.x} + i$
if $k < n_e$ **then**
 ▷ Gather information from neighbors
 $q_{e_1}[(0..n_v)] = q^t[id_{e_1}(t_x, k)]$
 $q_{e_2}[(0..n_v)] = q^t[id_{e_2}(t_x, k)]$
 ...
 ▷ Reconstruct left and right solutions
 $q_L[(0..n_v)] = f(q_{e_1}, q_{e_2}...)$
 $q_R[(0..n_v)] = f(q_{e_1}, q_{e_2}...)$
 ▷ Compute the interface flux
 $\text{InterfaceFlux}(q_L, q_R, f_n)$
 ▷ Store interface flux into global memory
 $f^g[k + (0..n_v) * n_f] = f_n[(0..n_v)]$
end if

Algorithm 2 DG_Interpolation

▷ Point on element face
 $t_x = \text{threadIdx.x}$
▷ Current face in block
 $t_y = \text{threadIdx.y}$
▷ The global face
 $f = \text{blockIdx.x} * \text{blockDim.y} + t_y$
if $f < n_f$ **then**
 ▷ Gather index information on face
 $m = id_f^t(t_x, f)$
 for $l = 0$ to n_{sp1d} **do**
 ▷ Read solution point information and operate
 $id = id_{sp}^t(m, l)$
 $q_l[(0..n_v)] = q_l[(0..n_v)] + c_{int}^t[l] * q^t[id]$
 end for
 $q_i^g[(t_x, f, 0..n_v)] = q_l[(0..n_v)]$
end if

Algorithm 3 DG_Couple

▷ Point on element face
 $t_x = \text{threadIdx.x}$
▷ Current face in block
 $t_y = \text{threadIdx.y}$
▷ The global face
 $f = \text{blockIdx.x} * \text{blockDim.y} + t_y$
if $f < n_f$ **then**
 ▷ Read data (normals, cell indexes)
 ...
 ▷ Read in left and right solution
 $q_L[(0..n_v)] = q^t[(id_{e_1}(t_x, f), 0..n_v)]$
 $q_R[(0..n_v)] = q^t[(id_{e_2}(t_x, f), 0..n_v)]$
 ▷ Compute the interface flux
 $\text{InterfaceFlux}(q_L, q_R, f_n)$
 ▷ Store interface flux into global memory
 $f_n^g[(t_x, f, 0..n_v)] = f_n[(0..n_v)]$
end if

Algorithm 4 DG_Flux

▷ Solution points, current element in block, global block
 $t_x = \text{threadIdx.x}$
 $t_y = \text{threadIdx.y}$
 $k = \text{blockIdx.x} * \text{blockDim.y} + t_y$
if $k < n_e$ **then**
 ▷ Read state at solution points
 $q[(0..n_v)] = q^t[(t_x, k, 0..n_v)]$
 ▷ Compute flux into shared memory
 $f^s[t_x, t_y, (0..n_v)] = F(q[(0..n_v)])$
 $g^s[t_x, t_y, (0..n_v)] = G(q[(0..n_v)])$
 ▷ Threads need to wait for shared memory to fill
 $\text{syncthreads}()$
 ▷ Compute volume integral using shared memory
 for $l = 0$ to n_{sp} **do**
 ▷ Stiffness matrix coefficients
 $(S_x, S_y) = (S_x^t, S_y^t)[(t_x, l)]$
 $\text{Vol}[(0..n_v)] = \text{Vol}[(0..n_v)] + V([S_x, S_y, f^s, f^g])$
 end for
 ▷ Surface integral next
 for $l = 0$ to n_{fp} **do**
 ▷ Read integration term
 $I = I^t[(t_x, l)]$
 ▷ Read in flux at interface points and compute surface integral
 $f_n[(0..n_v)] = f_n^t[(l, k, 0..n_v)]$
 $\text{Sur}[(0..n_v)] = \text{Sur}[(0..n_v)] - f_n[(0..n_v)] * I$
 end for
 ▷ Assemble flux derivative and store
 $\text{Res}^g[(t_x, k, 0..n_v)] = M^{-1} * (\text{Vol}[(0..n_v)] + \text{Sur}[(0..n_v)])$
end if

The *DG_Interpolation* kernel runs threads along each point in all the faces in the domain. At each face, the solution point information is read from texture memory, which serves as an index to read the required

state at the solution points. The solution states and interpolation coefficients (*cint*) are read from textured memory to perform the indicated operation, which is stored in global memory for future access. Note that *cint* is used in other algorithms to indicate interpolation coefficients, but the coefficients are not the same between the algorithms. To couple the elements, an even simpler kernel (*DG-Couple*), only demands the left and right information at interfaces, obtained in Algorithm 2. Boundary conditions are imposed on q_R if necessary.

In Algorithm 4, the threads run on solution points within elements, and multiple elements are packed within a thread block. A sufficient amount of shared memory is allocated for storage of the flux, and threads are halted while the memory is loaded. Shared memory in this case offers high computational efficiency, since the volume integration loop requires information at other solution points in the element. The surface integral is computed in a similar manner, without the use of shared memory. The flux derivative is assembled and stored in the GPU's global memory.

3.4.2 SD GPU

Like DG, SD also decomposes nicely into three separate kernels as shown in Fig. 2: Interpolations, coupling, and flux computation. Two major differences in implementation are the following: SD has no volume integration and each element has interior flux points (not just on the edges). This aspect makes the interpolation more expensive in terms of operations and storage, but the final flux evaluation cheaper.

Algorithm 5 SD-Interpolation

```

▷ Flux points in one direction
 $t_x = \text{threadIdx.x}$ 
▷ Current element in block
 $t_y = \text{threadIdx.y}$ 
▷ The global element
 $k = \text{blockIdx.x} * \text{blockDim.y} + t_y$ 
if  $f < n_e$  then
  ▷ Read states into shared memory
  if  $j < n_{sp}$  then
     $q^s[(t_x, t_y, 0..n_v)] = q^t[t_x, k, 0..n_v]$ 
  end if
  syncthreads()
  ▷ Build polynomial at flux points (x-direction)
  for  $l = 0$  to  $n_{sp1d}$  do
     $q_x[(0..n_v)] = q_x[(0..n_v)] + \text{cint}^t[l, t_x] * q^s[l, t_x, t_y, 0..n_v]$ 
  end for
  ▷ Compute flux terms
   $f_x[(0..n_v)] = F(q_x[(0..n_v)])$ 
  ▷ Store states and flux at flux points
   $q_{x,y}^g[(t_x, k, 0..n_v)] = q_x[(0..n_v)]$ 
   $f_{x,y}^g[(t_x, k, 0..n_v)] = f_x[(0..n_v)]$ 
  ▷ Repeat for y-direction
  ...
end if

```

The interpolation must be completed in each coordinate direction separately, and both the solution states and flux terms must be stored in global memory for future use. The *SD-Interpolation* kernel, outlined in Algorithm 5, sets each thread as a flux point in an element, and takes time to load the solution states into shared memory. Note that for SD, $n_{sp} < n_{fp}$, regardless of order of accuracy. This shared memory will be used for both interpolation in the x and y-directions. Once storage for x-coordinates are completed, the y-direction terms are computed. For the coupling of elements, the reader is referred back to Algorithm 3. Each element now has left and right solutions available in global memory access, and the DG algorithm can

be used to store the interface flux. The only difference is the location of that stored flux. Rather than f_n^g , it is simply stored in $f_{x,y}^g$, overwriting the original memory from the kernel *SD_Interpolation*.

Algorithm 6 SD_Flux

```

▷ Flux points in one direction ( $n_{sp1d} * n_{fp1d}$ )
 $t_x = \text{threadIdx.x}$ 
▷ Current element in the block and global element
 $t_y = \text{threadIdx.y}$ 
 $k = \text{blockIdx.x} * \text{blockDim.y} + t_y$ 
▷ Solution point and flux point indexes
 $isp = \text{mod}(t_x, n_{sp1d})$ 
 $ifp = t_x / n_{sp1d}$ 
if  $k < n_e$  then
  ▷ Read fluxes into shared memory
   $id_x = id_x^t(isp, ifp)$ 
   $id_y = id_y^t(isp, ifp)$ 
   $f_x^s[id_x, t_y, 0..n_v] = f_{x,y}^t[id_x, k, 0..n_v]$ 
   $f_y^s[id_y, t_y, 0..n_v] = f_{x,y}^t[id_y, k, 0..n_v]$ 
   $\text{syncthreads}()$ 
  ▷ Now only run on solution points
  if  $ifp < n_{sp1d}$  then
    ▷ Flux differentiation on solution points
    for  $l = 0$  to  $n_{fp1d}$  do
      ▷ Derivative coefficients
       $c_x = c_x[isp, l]$ 
       $c_y = c_y[ifp, l]$ 
      ▷ Flux derivative per direction
       $dF_x[0..n_v] = dF_x[0..n_v] + c_x * f_x^s[id_x, l, t_y, 0..n_v]$ 
       $dF_y[0..n_v] = dF_y[0..n_v] + c_y * f_y^s[id_y, l, t_y, 0..n_v]$ 
    end for
     $Res^g[t_x, k, 0..n_v] = dF_x[0..n_v] + dF_y[0..n_v]$ 
  end if
end if

```

The kernel *SD_Flux* (Algorithm 6) gathers all the flux terms and computes the derivative at the solution points. The threads are allowed to run across solution and flux points in one direction. This allows the flux to be loaded into shared memory in the two coordinate directions (x, y). The extra flux point thread is stopped, and the algorithm continues to run only on solution points. Implementations of the method were performed without shared memory, and threads only operated across solution points reading the flux values from textured memory. The presented algorithm was found to be around 1% faster. The derivative of the flux is completed across the flux points and stored at the solution points (these coefficients are all in c_x and c_y). The final results are written to global memory for time-stepping.

3.4.3 CPR / NDG CUDA

Both CPR and NDG methods have the unique property that solution and flux point coincide with one another, which enables the entire algorithm to be written in one GPU kernel, as outlined in Fig. 2. The major differences between the two methods are illustrated within the algorithm presented. For CPR, the solution states are loaded into memory, the **for** loop computes the solution derivatives, and the projections are computed and stored. NDG requires the flux values to be stored and the flux derivatives computed within the **for** loop.

Algorithm 7 CPR_Flux / (NDG_Flux) Part 1

```
▷ Max of flux points or solution points
 $t_x = \text{threadIdx.x}$ 
▷ Current element in the block and global element
 $t_y = \text{threadIdx.y}$ 
 $k = \text{blockIdx.x} * \text{blockDim.y} + t_y$ 
▷ Solution points in x and y directions
 $i_x = \text{mod}(t_x, n_{sp1d})$ 
 $i_y = t_y / n_{sp1d}$ 
if  $k < n_e$  then
  ▷ Operate on solution points first
  if  $t_x < n_{sp}$  then
    ▷ Only CPR - Load solution into shared memory from texture
     $q^s[(t_x, t_y, 0..n_v)] = q^t[(t_x, k, 0..n_v)]$ 
    ▷ Only NDG - Load solution from texture and store flux values
     $f^s[(t_x, t_y, 0..n_v)] = f(q^t[(t_x, k, 0..n_v)])$ 
    syncthreads()
    for  $l = 0$  to  $n_{sp1d}$  do
      ▷ Only CPR
       $c_x = c_x^t[(l, i_x)]$ 
       $c_y = c_y^t[(l, i_y)]$ 
       $dq_x[(0..n_v)] = dq_x[(0..n_v)] + c_x * q^s[(i_x, l, t_y, 0..n_v)]$ 
       $dq_y[(0..n_v)] = dq_y[(0..n_v)] + c_y * q^s[(i_y, l, t_y, 0..n_v)]$ 
      ▷ Only NDG
       $d_x = d_x^t[(l, i_x)]$ 
       $d_y = d_y^t[(l, i_y)]$ 
       $df_x[(0..n_v)] = df_x[(0..n_v)] + d_x * f^s[(i_x, l, t_y, 0..n_v)]$ 
       $df_y[(0..n_v)] = df_y[(0..n_v)] + d_y * f^s[(i_y, l, t_y, 0..n_v)]$ 
    end for
    ▷ Only CPR - Compute projections
     $Proj[(0..n_v)] = P(dq_x, dq_y)$ 
  end if
  syncthreads()
  ...
```

The algorithm sets threads to operate over flux points or solution points, whichever is larger (the algorithm can then switch to operating on the other set within the kernel). First, operations are completed over solution points, reading in the solution states and storing the states (flux values for NDG) into shared memory. The shared memory is used in computing derivatives of the states in CPR, or the flux for NDG. The chain rule is used for the flux derivative in CPR.

Algorithm 8 CPR_Flux / (NDG_Flux) Part 2

```

...
if  $t_x < n_{fp}$  then
  ▷ Couple elements (see DG_Couple)
  ...
  ▷ Store normal flux difference into shared memory ( $f^s$  for NDG)
   $q^s[(t_x, t_y, 0...n_v)] = f_x[(0...n_v)] * n_x + f_y[(0...n_v)] * n_y - f^n[(0...n_v)]$ 
end if
synctheads()
if  $t_x < n_{sp}$  then
  ▷ Get number of updates per solution point
   $n_{upd} = n_{upd}^t[t_x]$ 
  ▷ Correct the normal flux (Lift the flux for NDG)
  for  $l = 0$  to  $n_{upd}$  do
    ▷ Locations for correction (lifting)
     $id = id^t[(t_x, l, k)]$ 
    ▷ Only CPR
     $Corr[(0...n_v)] = Corr[(0...n_v)] - c^t[id] * q^s[(t_x, t_y, 0...n_v)]$ 
    ▷ Only NDG
     $Lift[(0...n_v)] = Lift[(0...n_v)] - L^t[id] * f^s[(t_x, t_y, 0...n_v)]$ 
  end for
  ▷ Only CPR
   $Res^g[(t_x, k, 0...n_v)] = Proj[(0...n_v)] + Corr[(0...n_v)]$ 
  ▷ Only NDG
   $Res^g[(t_x, k, 0...n_v)] = df_x[(0...n_v)] + df_y[(0...n_v)] + Lift[(0...n_v)]$ 
end if
end if

```

The second part of the algorithm switches the threads to operate on flux points. The coupling of the elements is straightforward, as information is already on element interfaces. The normal flux difference on the flux points is stored into the same shared memory space from Algorithm 7. The threads are switched a final time to operate on solution points, where, based on the method, the normal flux difference stored in shared memory is corrected or lifted and used to update the residual.

3.4.4 Shock Capturing

The shock capturing algorithm for FV differs significantly from the other methods. In Algorithm 1, the left and right states at element interfaces is computed. Immediately following this step, the solutions can be limited using an appropriate slope limiting routine following second or third order MUSCL reconstruction.

Unlike the FV method, the approach used in high-order methods requires extra sweeps through the computational domain. The slope limiting requires solution averages at elements, hence the high-order methods must first build the averaged solution within each element before any slope limiting can be applied.

Algorithm 9 Average

```
▷ The current solution state
 $t_x = \text{threadIdx.x}$ 
▷ The current element in the block
 $t_y = \text{threadIdx.y}$ 
▷ Current global element
 $k = \text{blockIdx.x} * \text{blockDim.y} + t_y$ 
if  $k < n_e$  then
  for  $l = 0$  to  $n_{sp}$  do
    ▷ Build average
     $q_m[t_x] = c_m^t[l] * q^t[(t_x, l, k)]$ 
  end for
   $q_m^g[(t_x, k)] = q_m[t_x]$ 
end if
```

The *Average* kernel (Algorithm 9) builds the solution averages using information from texture memory and stores the result in global memory space. These averages are used in *Limit* kernels (Algorithms 10 and 11) for limiting.

Algorithm 10 Limit Part 1

```
▷ Solution points
 $t_x = \text{threadIdx.x}$ 
▷ The current element in the block
 $t_y = \text{threadIdx.y}$ 
▷ Current global element
 $k = \text{blockIdx.x} * \text{blockDim.y} + t_y$ 
if  $k < n_e$  then
  ▷ Run through points on edges
  if  $j < n_{ep}$  then
    ▷ Interpolate to edge if necessary
     $q_l = \dots$ 
    ▷ Load index locations of neighboring elements
     $(i_1, i_2) = \dots$ 
    ▷ Construct the minmod at the edge
     $q_e = q_m^t[k] + \text{minmod}(q_m^t[k] - q_l, q_m^t[i_2] - q_l, q_m^t[k], q_m^t[k] - q_m^t[i_1])$ 
    ▷ Check if solution is large
    if  $|q_l - q_e| > \epsilon$  then
       $mark = 1$ 
    end if
    ▷ Store the mark into shared memory at edge
     $tmp_s[(t_x, t_y)] = mark$ 
     $\text{syncthreads}()$ 
    ...
  end if

```

The *Limit Part 1* kernel starts by switching the threads to run on the edge points of elements. At each edge point, the solution is read from memory (CPR or NDG) or is interpolated from solution point information (DG or SD). Then the minmod limiter is applied at the edge to detect if the element has a discontinuity, and if there is one, the

Algorithm 11 Limit Part 2

```
...
mark = 0
▷ Each edge point runs through the others edge points
for  $l = 0$  to  $n_{ep}$  do
    mark = mark +  $tmp_s[l, t_y]$ 
end for
 $mark_s[t_y] = mark$ 
end if
synctreads()
if  $j < n_{sp}$  then
    if  $mark_s[t_y] > 0$  then
        ▷ Apply slope limiting now
        ...
    end if
end if
end if
```

Every edge point needs to see the markings of the others, which is completed using a summation. This way, an element with at least one troubled point will give each edge point a value of one. The marking is sent into shared memory so the information can be communicated when the threads switch to operate across the solution points. At each solution point, in shared block t_y , the marking is read from the shared space, and slope limiting is applied if this marking is greater than zero.

4 Results

Two test cases are presented for both a smooth and discontinuous problem. For all methods, a three state Runge-Kutta [34] time stepping scheme was applied and the interface fluxes were evaluated using the Rusanov [35] Riemann solver. The time step for each method was computed using the *CFL* condition as

$$\Delta t \leq \frac{CFL \Delta x}{|u| + c}. \quad (36)$$

The *CFL* number for high-order methods is known to be quite restrictive in comparison to FV. To ensure a fair comparison with FV, the following convention is used: At the end of a simulation, the error is recorded. A new simulation is completed at a value of $0.5 * CFL$ of the previous. Again, the error is recorded. If the percent error between these two errors is less than 0.1%, the *CFL* is termed the maximum *CFL*. Errors were completed by comparing the averaged solution with the averaged exact solution. For P^2 FV, the error was computed by reconstructing the solution along element faces, and then using a quadrature rule to compute an averaged solution [1]. Finally, since FV has one solution state per element, while high-order methods have multiple, the total number of degrees of freedom *NDof* between the methods was held constant. Only quadrilateral elements are considered in this work. For one element and a P^2 reconstruction for a high-order method, $NDof = 9$. To match this, the FV method must have 9 elements.

A single Tesla K20c GPU card was used for all simulations. The code was compiled under compute architecture 3.5 using the CUDA toolkit version 6.0. In addition, the `-O3` compiler optimization was used as well as the CUDA 64-bit libraries. Double precision is used for all computations. The computational time was nondimensionalized by taubench [36] using the following taubench condition:

```
./Taubench -n 250000 -s 10.
```

On the GPU workstation used in our simulations, taubench gave a value of 8.274. This produces what is known as a work unit, as suggested by the 1st International Workshop on High-Order Methods [1] when comparing timings from numerical methods. A work unit is a nondimensionalized unit computed by dividing the computational time it takes to complete a simulation by the taubench result.

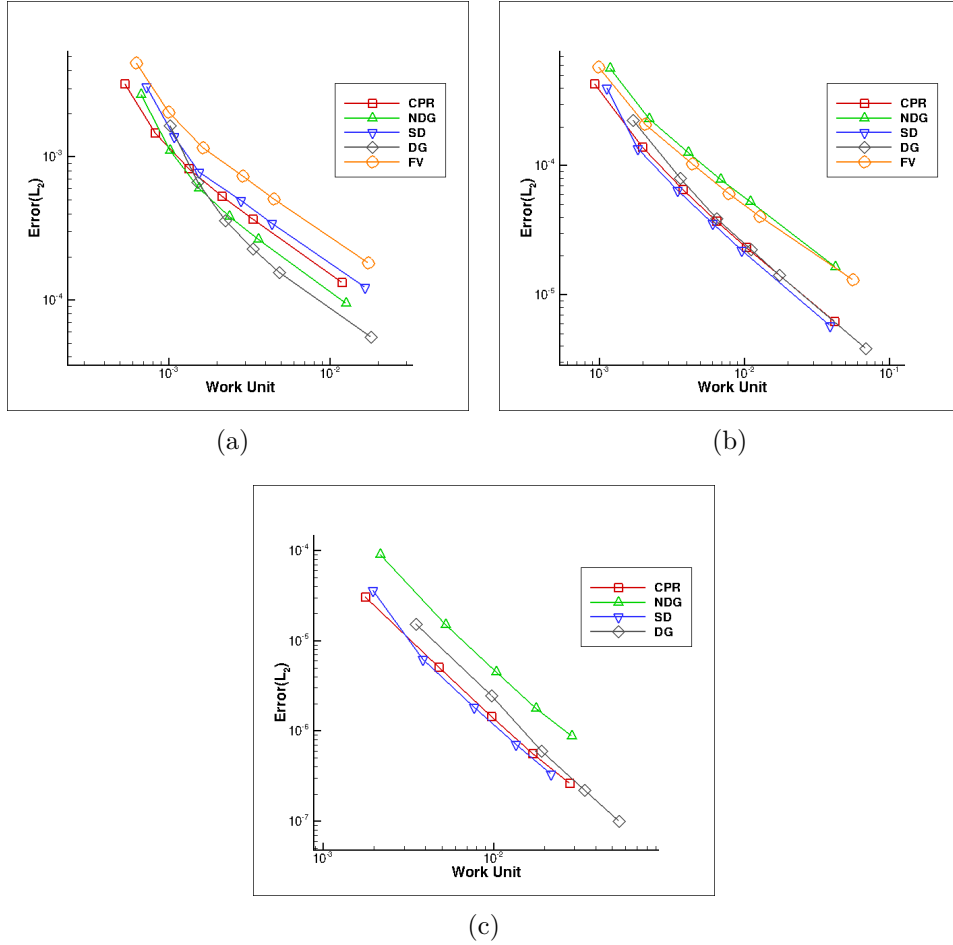


Figure 3: L_2 density errors using (a) P^1 , (b) P^2 , and (c) P^3 reconstructions versus work unit

4.1 Smooth Problem

A vortex propagation case is used as the smooth problem in this paper. The flow of the vortex is characterized in Ref. [37]. A mean flow is specified $(\rho, u, v, p) = (1, 1, 0, 1)$ with fluctuation in the velocity, temperature (T), and entropy (S),

$$\begin{aligned}
 (\delta u, \delta v) &= \frac{\epsilon}{2\pi} e^{0.5(1-r^2)} (-y, x), \\
 \delta T &= -\frac{(\gamma-1)\epsilon^2}{8\gamma\pi^2} e^{1-r^2}, \\
 \delta S &= 0.
 \end{aligned}$$

Here, $r^2 = x^2 + y^2$ and the vortex has strength $\epsilon = 5$. An exact solution exists and can be found using $x_e = x - ut$ and $y_e = y - vt$, where t is the final time. The solution evolves until time $t = 1$ and the L_2 error norm of ρ is computed. The domain is taken as $[-5, 5] \times [-5, 5]$ and periodic conditions are imposed on the boundaries. Discretizations from 20×20 to 100×100 quadrilateral elements are used in the simulations. Table 1 shows the maximum CFL chosen for the runs, which allowed a less than 0.1% error change when the CFL was decreased by 1/2.

The solution errors versus work units for P^1 , P^2 , and P^3 reconstructions are shown in Fig. 3. The overall trend of increasing accuracy with increasing work unit is observed for all methods. It is observed that the high-order methods obtain smaller error thresholds than the FV method for a given work unit

Table 1: Maximum CFL - Smooth problem

P^1 —DoFs	CPR	NDG	SD	DG	FV
1600	0.24	0.24	0.3	0.24	0.4
3600	0.24	0.24	0.3	0.24	0.4
6400	0.24	0.24	0.3	0.24	0.38
10000	0.24	0.24	0.3	0.24	0.38
14400	0.24	0.24	0.3	0.24	0.37
P^2 —DoFs	CPR	NDG	SD	DG	FV
3600	0.14	0.14	0.2	0.14	0.4
8100	0.13	0.13	0.2	0.13	0.4
14400	0.13	0.13	0.2	0.13	0.38
22500	0.13	0.13	0.2	0.13	0.37
32400	0.13	0.13	0.2	0.13	0.37

(exception for P^2 NDG, which has larger errors associated). For P^1 reconstructions shown in Fig. 3 (a), DG clearly outperforms other methods, but as the order is increased, Fig. 3 (b) shows CPR and SD both achieve comparable errors with DG for a given work unit. In the case of CPR, the schemes compact nature is attributed to this, where the operations to compute the flux derivative are contained in one GPU kernel. For SD, Table 1 shows that the SD method can take larger time-steps than the other high-order methods, as the CFL is not as restrictive. Similar plots are observed in the comparative study done by Yu *et al.* [23], where the error is compared with work units for several high-order methods on CPUs. They also observe that CPR has a considerably lower error given a work unit for P^2 reconstruction than other methods, while NDG is significantly higher. In the results presented here, SD is comparable to CPR because the maximum allowable time-step for a given temporal error is used. This is different than the approach in Ref. [23], where a constant time-step is implemented. A fourth order reconstruction is also completed, and shown in Fig. 3 (c). It illustrates that the SD and CPR methods both obtain the lowest errors for a given work unit for a P^3 reconstruction.

Figure 4 shows the work unit needed to complete a simulation on a given mesh for P^1 , P^2 , and P^3 reconstructions. The obvious trend of the work unit increasing for finer meshes is observed for both orders of accuracy. To complete a full simulation, the FV and CPR methods are the fastest on coarse meshes (Fig. 4 (a) and (b)). Small computational domains do not take advantage of the GPU architecture with the optimizations and different memory types discussed in this paper. As the domain is refined and the order is, the high-order schemes can produce solutions faster than FV. The data illustrates that on fine meshes with high-order reconstruction, the high-order CPR, NDG, and SD methods run faster than the FV method as the degrees of freedom are increased.

Further increasing the order to P^3 , Fig. 4 (c), shows the CPR and NDG converge to the same work unit for a given simulation. The SD method, however, is able to complete solutions faster than any other high-order method for P^3 reconstruction. The solution errors are recorded for the high-order methods and are shown in Tables 2 and 3. For P^1 reconstructions, the DG method produces the lowest L_2 errors and all methods slopes decay at a rate equivalent to the order of accuracy. A similar trend is observed for P^2 errors. Note that the NDG errors are significantly higher, which is due to aliasing issues with the method.

4.2 Discontinuous Problem

The next case is a radially expanding shock tube from Toro [38]. A domain of size $[-1, 1] \times [-1, 1]$ initializes density and pressure (ρ, p) of 1.0 inside a radius of 0.4. Outside the radius, $\rho = 0.125$ and $p = 0.1$. There is no velocity component at the initial time. Rather than using solution errors to check if the CFL is small enough, the residual error is used. The solution is ran until a final time of $t = 0.25$, where the density is compared along the centerline, $y = 0$. For the reference solution, the data was taken from the text Riemann Solvers and Numerical Methods for Fluid Dynamics [38] (digitized for use here). As illustrated in Fig. 5 (b), all methods have good agreement with the reference solution.

Table 2: High-order error values for smooth problem (P^1 reconstruction)

Method	CPR Error	CPR Slope	NDG Error	NDG Slope
20×20	3.21E-003	-	2.70E-003	-
30×30	1.46E-003	1.94	1.10E-003	2.22
40×40	8.25E-004	1.98	6.04E-004	2.07
50×50	5.29E-004	1.99	3.83E-004	2.04
60×60	3.67E-004	2.00	2.65E-004	2.02
Method	SD Error	SD Slope	DG Error	DG Slope
20×20	3.07E-003	-	1.65E-003	-
30×30	1.38E-003	1.96	6.63E-004	2.24
40×40	7.78E-004	2.00	3.59E-004	2.13
50×50	4.96E-004	2.02	2.26E-004	2.08
60×60	3.44E-004	2.02	1.55E-004	2.06

Table 3: High-order error values for smooth problem (P^2 reconstruction)

Method	CPR Error	CPR Slope	NDG Error	NDG Slope
20×20	4.30E-004	-	5.63E-004	-
30×30	1.38E-004	2.81	2.30E-004	2.20
40×40	6.51E-005	2.60	1.26E-004	2.10
50×50	3.69E-005	2.55	7.81E-005	2.14
60×60	2.32E-005	2.55	5.23E-005	2.19
Method	SD Error	SD Slope	DG Error	DG Slope
20×20	4.00E-004	-	2.24E-004	-
30×30	1.36E-004	2.66	7.95E-005	2.55
40×40	6.40E-005	2.62	3.90E-005	2.48
50×50	3.57E-005	2.62	2.24E-005	2.48
60×60	2.21E-005	2.62	1.42E-005	2.50

Table 4: Maximum CFL - Discontinuous problem

P^1 —DoFs	CPR	NDG	SD	DG	FV
160k	0.2	0.2	0.3	0.22	0.58
640k	0.2	0.2	0.27	0.2	0.58
P^2 —DoFs	CPR	NDG	SD	DG	FV
360k	0.1	0.1	0.18	0.08	0.54
1440k	0.1	0.1	0.18	0.08	0.54

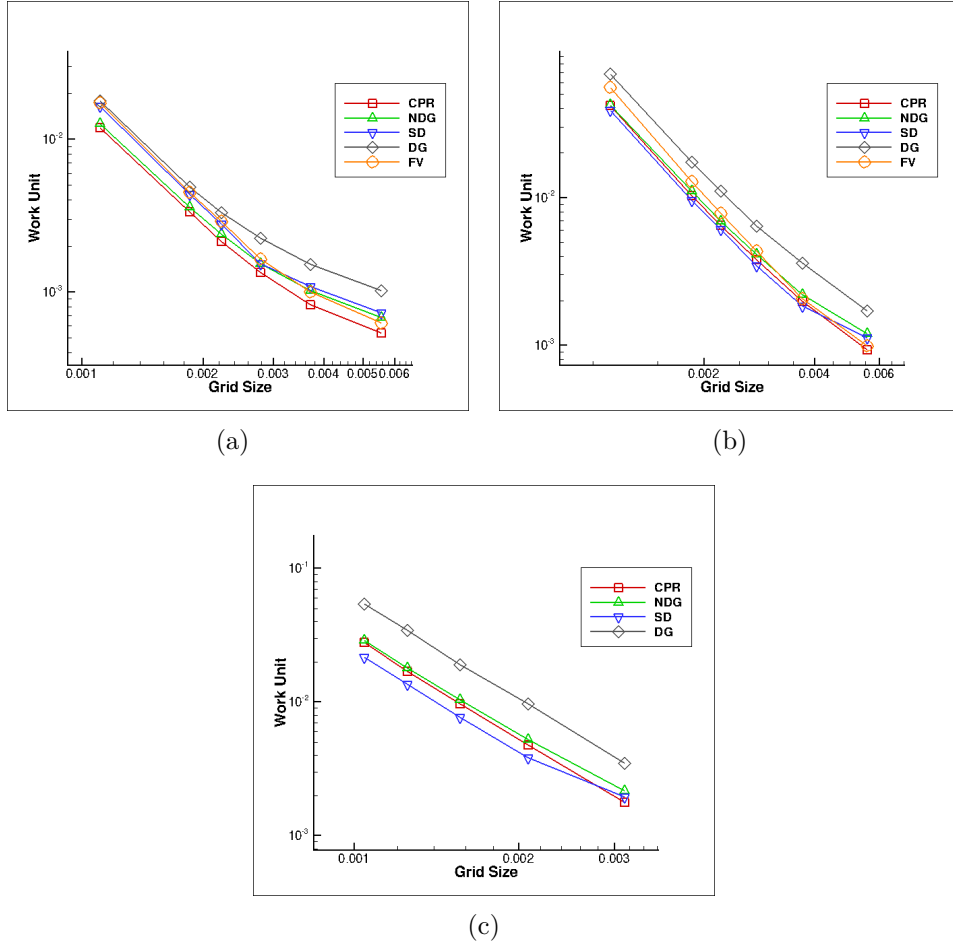


Figure 4: Total work unit to finish simulations for (a) P^1 , (b) P^2 , and (c) P^3

Fig. 6 illustrates the work unit needed per iteration for each method for both P^1 and P^2 reconstructions. As the computational domain is increased, the benefit of using some high-order methods becomes apparent. For the P^2 reconstruction in Fig. 6 (b) with 1440k degrees of freedom, CPR is 27% faster per iteration than FV, while DG is 14% slower than FV.

The total computational work is shown in Fig. 7 and 8. For P^1 reconstructions, the CPR method is the fastest of the high-order methods, while SD and DG take the most time. Once the reconstruction is increased to P^2 , a similar trend is observed, however the total work for SD and CPR is nearly identical. This is due to the SD schemes ability to take larger time steps than the CPR approach. However, the time step restrictions on high-order methods are harsher than FV, which enables FV to arrive at the final solution time 25% faster than the CPR/SD schemes for a P^2 reconstruction with 1440k degrees of freedom. This is also the case because of the extra sweeps the high-order methods need to take for discontinuous problems, one for evaluating the average and another to apply the limiting procedure.

5 Conclusions

The presented work compares multiple numerical methods implemented on GPUs using CUDA computing. The algorithms for each method were presented, and used to test smooth and discontinuous problems. The maximum allowable time step from the CFL condition was used for each problem, with the number of degrees of freedom held constant across the methods. For the smooth problem, the high-order methods obtained an

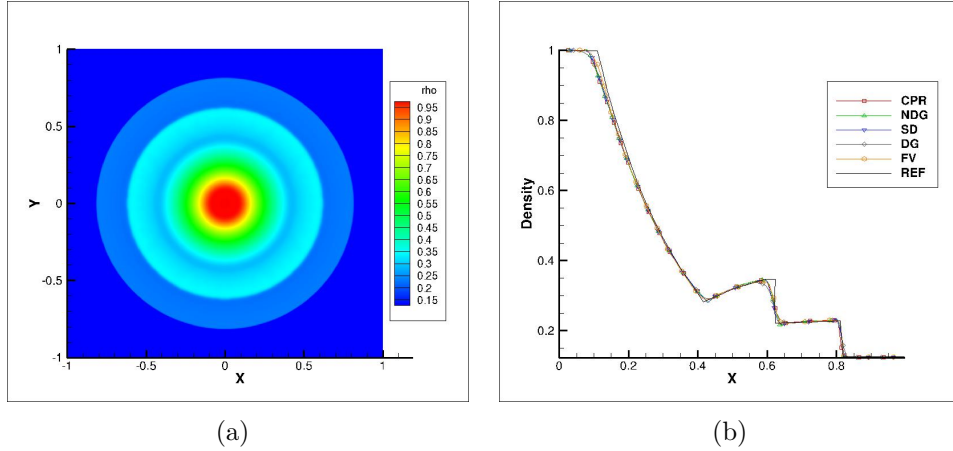


Figure 5: Discontinuous test case results (a) Density contours (b) P^1 solution comparison

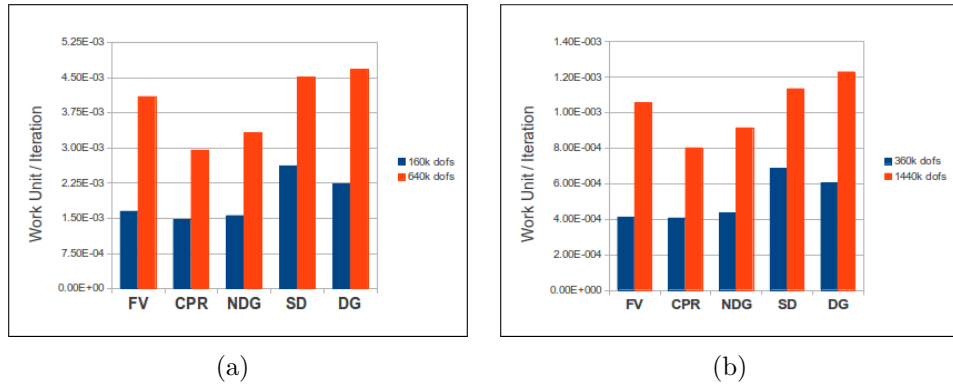


Figure 6: Computational work per iteration for (a) P^1 and (b) P^2 reconstruction

error threshold at a lower work unit than the FV method. Additionally, the CPR, NDG, and SD methods are capable of arriving at solutions faster than the FV approach as the computational domain is increased. For discontinuous problems, the FV method does produce solutions 25% faster than the fastest high-order methods, but solution profiles between the methods are similar. The computational work per step shows the CPR and NDG methods are most efficient, but time-step restrictions cause slower solution generation when compared to FV.

This two-dimensional approach may provide a foundation for comparisons with three-dimensional methods. The extension is necessary because bottlenecks shift when going from two-dimensional to three-dimensional problems. Additionally, different grids and unstructured mesh cases should be considered.

Acknowledgements

This research has been supported by a NIAC (NASA Innovative Advanced Concepts) Phase 2 study entitled “An Innovative Solution to NASA’s Asteroid Impact Threat Mitigation Grand Challenge and Its Flight Validation Mission Design.” Additional support has been given by the Vance Coffman Chair Fund. Approved for unlimited release: LA-UR-17-27957.

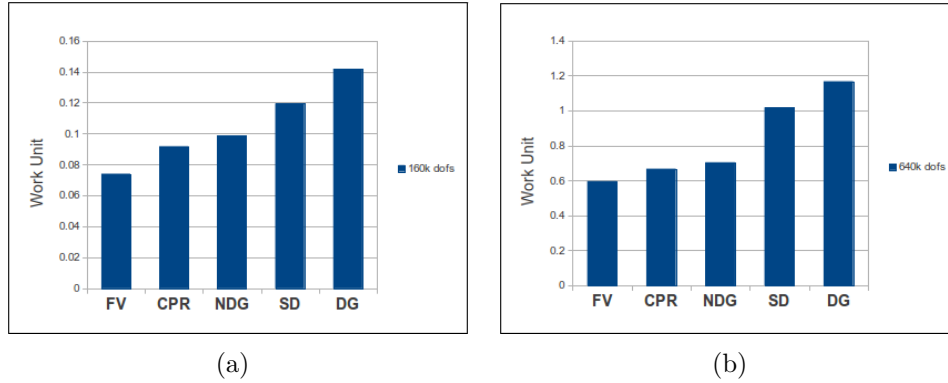


Figure 7: Total work for P^1 reconstruction (a) 160,000 degrees of freedom and (b) 640,000 degrees of freedom

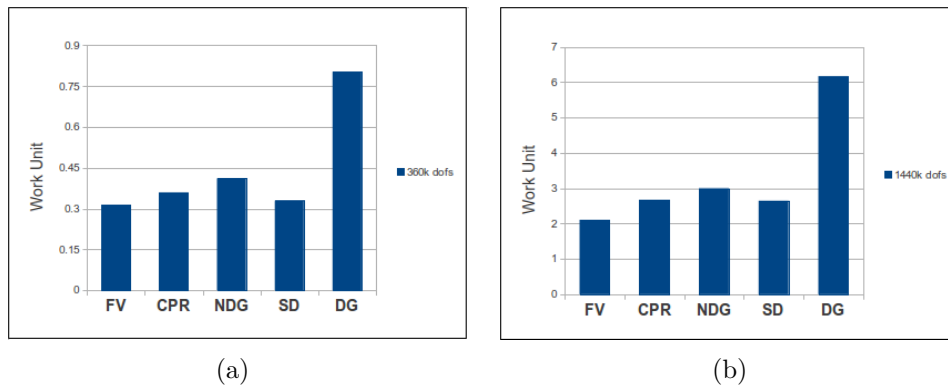


Figure 8: Total work for P^2 reconstruction (a) 360,000 degrees of freedom and (b) 1,440,000 degrees of freedom

References

- [1] Z. J. Wang *et al.*, Int J Numer Methods Fluids **72**, 811 (2013).
- [2] Z. J. Wang and H. Gao, J Comput Phys **178**, 210 (2002).
- [3] M. Castro, S. Ortega, M. de la Asunción, J. M. Mantas, and J. M. Gallardo, High Performance Computing **339**, 165 (2011).
- [4] K. Obenschain, K. Corrigan, and G. Patnaik, AIAA (2011).
- [5] F. Bassi and S. Rebay, J Comput Phys **138**, 251 (1997).
- [6] C. E. Baumann and T. J. Oden, J Numer Meth Fluids **31**, 79 (1999).
- [7] B. Cockburn and C. W. Shu, J Comput Phys **141**, 199 (1998).
- [8] B. Cockburn and C. W. Shu, Math Comput **52**, 411 (1989).
- [9] B. Cockburn, S. Lin, and C. W. Shu, J Comput Phys **84**, 90 (1989).
- [10] W. H. Reed and T. R. Hill, Los Alamos Scientific Laboratory Report, 1973 (unpublished).
- [11] J. S. Hesthaven and T. Warburton, *Nodal Discontinuous Galerkin Methods: Algorithms, Analysis, and Applications*. (Springer-Verlag, New York, 2008).
- [12] A. Klöckner, T. Warburton, J. Bridge, and J. S. Hesthaven, J Comput Phys **228**, 7863 (2009).

- [13] H. T. Huynh, AIAA (2007).
- [14] Z. J. Wang, *Adaptive High-Order Methods in Computational Fluid Dynamics* (2011).
- [15] Z. J. Wang and H. Gao, J Comput Phys **228**, 8161 (2009).
- [16] M. L. Yu and Z. J. Wang, J Sci Comput **54** (1), 227 (2013).
- [17] M. Hoffmann, C.-D. Munz, and Z. J. Wang, ICCFD (2012).
- [18] B. J. Zimmerman and Z. J. Wang, Comput Fluids **101**, 263 (2014).
- [19] Y. Liu, M. Vinokur, and Z. J. Wang, J Comput Phys **216**, 780 (2006).
- [20] G. May and A. Jameson, AIAA (2006).
- [21] Y. Sun and Z. J. Wang, J Comput Phys **2**, 301 (2007).
- [22] B. J. Zimmerman, Z. J. Wang, and M. Visbal, AIAA (2013).
- [23] M. L. Yu, Z. J. Wang, and Y. Liu, J Comput Phys **259**, 75 (2014).
- [24] B. Van Leer, J Comput Phys **14**, 361 (1974).
- [25] B. Van Leer, J Comput Phys **32**, 101 (1979).
- [26] A. Harten, B. Enquist, S. Osher, and S. R. Chagrarvarthy, J Comput Phys **71**, 231 (1987).
- [27] B. Cockburn and C. W. Shu, J Sci Comput **16**, 173 (2001).
- [28] E. Kubatko, C. Dawson, and J. Westerink, J Comput Phys **227**, 9697 (2008).
- [29] O. C. Zienkiewicz and R. C. Taylor *The Finite Element Method the Basics* Vol. 1 (2000).
- [30] J. C. Tannehill, A. A. Anderson, and R. H. Pletcher *Computational Fluid Mechanics and Heat Transfer* Vol. 2 (1997).
- [31] P. L. Roe, Rev in Fluid Mech **18**, 337 (1986).
- [32] *NVIDIA CUDA C Programming Guide* Vol. 5.0 (2012).
- [33] B. J. Zimmerman, The efficient implementation of correction procedure via reconstruction with GPU computing, Master's thesis, Iowa State University, 2013.
- [34] C. W. Shu, SIAM J Sci Stat Comput **9**, 1073 (1988).
- [35] V. V. Rusanov, J Comput Math Phys **USSR(1)**, 267 (1961).
- [36] Taubench.
- [37] C. W. Shu, *Essentially non-oscillatory and weighted essentially non-oscillatory schemes for hyperbolic conservation laws, in: Advanced Numerical Approximation of Nonlinear Hyperbolic Equations* (Springer-Verlag, Berlin/New York, 1998).
- [38] E. F. Toro, *Riemann Solvers and Numerical Methods for Fluid Dynamics: A Practical Introduction* (Springer, London/New York, 2009).